# Distinct vertical structures of global eddy heat and salt transports revealed by altimetry and Argo observations

Xiangpeng Wang[1, 2], Xiaoming Zhai[2], Helen L. Johnson[3], J. H. LaCasce[4], Qinbiao Ni[5*], Yan Du[1, 6*]

1. Guangdong Provincial Key Laboratory of Ocean Remote Sensing and Big Data, State Key Laboratory of Tropical Oceanography, South China Sea Institute of Oceanology, Chinese Academy of Sciences, Guangzhou, China.

2. School of Environmental Sciences, Centre for Ocean and Atmospheric Sciences, University of East Anglia, Norwich, UK.

3. Department of Earth Sciences, University of Oxford, Oxford, UK

4. Department of Geosciences, University of Oslo, Oslo, Norway.

5. Southern Marine Science and Engineering Guangdong Laboratory (Zhuhai), Zhuhai, China

6. College of Marine Science, University of Chinese Academy of Sciences, Beijing, China.

*Corresponding author: Yan Du (duyan@scsio.ac.cn); Qinbiao Ni (niqinbiao@outlook.com)

**Key Points**

1. Global 3D structures of meridional eddy heat and salt transports are reconstructed from 25 years of altimetry and Argo data.
2. Eddy heat transport reverses with depth, while eddy salt transport exhibits a latitude-dependent pattern.
3. These contrasting behaviors highlight distinct roles of eddy heat and salt transports in the global oceanic heat and salt balance.

**Abstract:** Mesoscale eddies play a key role in redistributing oceanic heat and salt, yet their global three-dimensional (3D) transport structures remain poorly understood. Here, we estimate global meridional eddy heat and salt transports in the upper 1800 m from satellite altimeter and Argo observations, revealing distinct vertical structures. Eddy heat transport reverses with depth, being poleward in the upper ocean but equatorward below, resulting in strong vertical cancellation and a weak net contribution to total meridional heat transport. In contrast, eddy salt transport exhibits pronounced latitude dependence, weakly equatorward at low latitudes but strongly poleward at mid-latitudes, where it contributes nearly half of the total meridional salt transport. These contrasting behaviors primarily arise from differences in background temperature and salinity gradients, consistent with down-gradient eddy fluxes. Our results provide novel observational insights into the global 3D structures of eddy heat and salt transports, offering a benchmark for evaluating ocean and climate models.

**Plain Language Summary**

Ocean eddies are rotating currents found throughout the global ocean. They play an important role in transporting heat and salt, helping shape ocean circulation and climate. However, how these transports vary with depth remains poorly understood because observations below the surface are limited. By combining 25 years of satellite altimetry with Argo profiling data, we develop a new method for estimating the three-dimensional structure of ocean eddy heat and salt transports in the upper 1800 m of the global ocean. We find that heat transport by eddies changes direction with depth, leading to cancellation when vertically averaged. In contrast, eddy salt transport shows a clear latitude-dependent pattern and contributes significantly to the total meridional salt transport. These results show that ocean eddies transport heat and salt differently and highlight their distinct roles in the global climate system.

## 1. Introduction

Mesoscale eddies are ubiquitous features in the global ocean, with horizontal scales of tens to hundreds of kilometers and lifetimes of weeks to months, accounting for nearly 90% of oceanic kinetic energy (Aiki et al., 2016; Chelton et al., 2011; Pascual et al., 2006). Through nonlinear

processes such as trapping and stirring, these eddies induce substantial transports of heat, salt, and other tracers (Dong et al., 2014; Dufour et al., 2015; Yang et al., 2025). The magnitudes of these eddy-induced transports are comparable to those of large-scale wind- and thermohaline-driven circulation, thereby exerting a profound influence on regional and global climate (Frenger et al., 2015; Li et al., 2025; Zhang et al., 2014a).

Despite their importance, the three-dimensional (3D) structure of eddy heat and salt transports remains poorly quantified. A primary limitation is the scarcity of subsurface observations, which has led most previous estimates to rely on either satellite observations or numerical models. However, satellite observations provide only surface information, limiting their applicability to the sea surface or mixed layer (Melnichenko et al., 2021; Wang et al., 2023; Yang et al., 2025). Numerical models offer insights into subsurface eddy transports but have largely focused on depth-integrated fluxes rather than resolving their full vertical structure (Delman and Lee, 2021; Tréguier et al., 2014; Volkov et al., 2008). Moreover, recent studies show that even eddy-resolving global climate models exhibit substantial discrepancies with observations, leading to large uncertainties in eddy heat and salt fluxes (Beech et al., 2022; Chassignet et al., 2020; Ding et al., 2022). Reliable observational constraints are thus essential for assessing model biases and improving eddy parameterizations in ocean–climate models (Griffies et al., 2015).

Since the launch of the Argo program, more than two million temperature and salinity profiles have been collected in the upper 2000 m of the global ocean. However, the lack of concurrent subsurface velocity observations remains a major obstacle to quantifying global 3D eddy heat and salt transports. To address this, some studies estimated eddy transports by combining the temperature (salinity) anomalies within eddies with their propagation speeds, assuming complete trapping (Dong et al., 2014; Dong et al., 2017; Mo et al., 2024). However, recent Lagrangian analyses argued that eddy trapping accounts for only a fraction of the total lateral eddy transport, as substantial leakage occurs during eddy propagation. Instead, lateral transport is largely dominated by incoherent stirring and filamentation outside eddy cores (Abernathey and Haller, 2018; Liu et al., 2022; Sun et al., 2019; Xia et al., 2022).

Previous work suggests that mesoscale eddies exhibit distinct vertical structures (Steinberg et al., 2025; Zhang et al., 2013), enabling the downward projection of altimeter-derived surface

geostrophic currents. Several approaches have been developed, including traditional barotropic and baroclinic modes (Wunsch, 1997), the surface quasi-geostrophic (SQG) framework (Isern-Fontanet et al., 2008; LaCasce, 2012; LaCasce and Mahadevan, 2006), and the "surface mode" that accounts for rough bottom topography (de La Lama et al., 2016; LaCasce, 2017; LaCasce and Groeskamp, 2020). These methods, however, rely on idealized dynamical assumptions and may not fully capture the observed variability of eddy vertical structures. Recently, Ni et al. (2023) proposed a composite-eddy-structure method that empirically integrates altimetry and Argo data to project surface eddy velocities into the ocean interior, showing better agreement with moored current-meter observations than the aforementioned dynamical methods.

Here, we extend the composite-eddy-structure framework to reconstruct the subsurface eddy velocities, and integrate them with collocated Argo temperature and salinity profiles to estimate time-mean global 3D eddy transports. The results reveal distinct vertical structures of eddy heat and salt transports, highlighting their roles in regulating the oceanic heat and salt balance and providing a new observational benchmark for evaluating and improving ocean–climate models.

## 2. Data and methods

### 2.1 Data

Daily altimetric sea level anomaly (SLA) data for 1998–2022 are obtained from the Copernicus Marine Environment Monitoring Service (CMEMS). This dataset merges multiple satellite altimetry records and is distributed on a global 1/4° × 1/4° grid. To remove large-scale signals associated with heating, cooling, and wind forcing while retaining mesoscale eddy signals, each SLA map is spatially high-pass filtered using a Gaussian function with a half-power cutoff wavelength of 20° (Chelton et al., 2011; Ni et al., 2023).

Argo profiles for the same 25-year period are obtained from the China Argo Real-time Data Center. All Argo profiles used in this study are delayed-mode data that have undergone standard quality control, including salinity drift correction, and only thoes with quality flag = 1 are retained. In total, over 2.1 million temperature and salinity profiles are collected over the global ocean, with 82% of 2° × 2° bins containing more than 100 profiles, ensuring broad spatiotemporal coverage (Supplementary Figure S1). Each profile is linearly interpolated to 10-m intervals between 10 and

1800 m.

The CORE.2 global monthly air–sea flux dataset (Large & Yeager, 2009), with 1° × 1° spatial resolution, is used to derive climatological heat and freshwater fluxes and to estimate oceanic total heat and salt transports. Surface fluxes in this dataset are based on NCEP reanalysis, adjusted with satellite and in situ observations, and computed using bulk parameterizations.

**2.2 Composite eddy vertical structures**

Mesoscale eddies are first identified from high-pass filtered SLA maps, with the eddy center corresponding to the local SLA extremum and the eddy boundary determined by the outermost closed contour (Chelton et al., 2011). Argo profiles within 2r of the eddies (where r is the eddy radius) are used to construct eddy vertical structures. The eddy-induced pressure anomaly ($P'$) is calculated by integrating the hydrostatic equation downward from the surface:

$$P'(z) = \rho_{top} g\eta' + \int_z^0 \rho' g dz, \quad (1)$$

where $\rho_{top}$ is the shallowest potential density, $g$ is the gravitational acceleration, $\eta'$ is the high-pass-filtered SLA at the location of the Argo profile, and $\rho'$ is the potential density anomaly profile obtained by subtracting a local monthly climatology. The pressure anomalies of Argo profiles are objectively interpolated onto a normalized eddy coordinate system (0.1r × 0.1r) and composited on a global 2° × 2° grid using 10° × 10° bins centered at each grid point, ensuring sufficient profiles for robust analysis. Since the vertical pressure anomalies induced by cyclonic and anticyclonic eddies are similar in shape but opposite in sign (Supplementary Figure S2b-e), the sign of the pressure anomaly profiles associated with cyclonic eddies is reversed before the composite analysis. The eddy vertical structure function, $F(z)$, at each grid point is obtained by horizontally averaging the composite eddy pressure anomalies within one eddy radius and normalizing by its surface value:

$$F(z) = \frac{\overline{P'_z(r)}}{\overline{P'_0(r)}}. \quad (2)$$

The composite results show that eddy structures are surface-intensified in the tropics but extend deeper in mid- and high latitudes, consistent with previous studies (Supplementary Figure S2f; Ni et al., 2023; Steinberg et al., 2025). Comparison with moored current-meter data confirms that these composites capture the dominant mode of eddy variability (Supplementary Figure S3),

providing a robust empirical basis for projecting altimeter-derived surface eddy velocities into the ocean interior. Further details of the eddy composite procedure can be found in Ni et al. (2023).

### 2.3 Subsurface eddy velocities

The meridional component of surface eddy velocity is computed from SLA data using geostrophic balance:

$$v_0' = \frac{g}{f}\frac{\partial \eta'}{\partial x}, \quad (3)$$

where $f$ is the Coriolis parameter. Subsurface geostrophic velocities at each Argo profile are then obtained by projecting the surface eddy velocity downward using the nearest composite eddy structure function:

$$v'(z) = v_0' \cdot F(z). \quad (4)$$

### 2.4 Meridional eddy heat and salt transports

The meridional eddy heat and salt transports ($Q_e, F_e$) are computed as:

$$Q_e(z) = \rho_0 C_\rho \overline{v'(z)\, T'(z)}, \quad (5)$$

$$F_e(z) = \overline{v'(z)\, S'(z)}, \quad (6)$$

where $\rho_0$=1025 kg m$^{-3}$ is the reference density, $C_\rho$=4200 J kg$^{-1}$ °C$^{-1}$ is specific heat capacity of sea water, and $T'$ and $S'$ are eddy-induced temperature and salinity anomalies relative to the monthly climatology. The overbar denotes a 25-year time average. Eddy transport estimates for individual Argo profiles are averaged within global 2° × 2° bins. Regions within ±5° latitude of the equator are excluded, as geostrophic balance is invalid near the equator. Sensitivity of the bin size is shown in Supplementary Figure S4. Results based on 1° × 1° grids show some patchiness, but this is considerably reduced using 2° × 2° grids, with only minor changes when the resolution is further coarsened to 3° × 3° grids. Based on this assessment, a 2° × 2° grid is adopted as the optimal choice, balancing spatial resolution and sampling robustness.

Since Argo profiles are spatially and temporally discrete, $T'$ and $S'$ cannot be spatially high-pass filtered to fully match the mesoscale variability retained in $v'$. Consequently, $T'$ and $S'$ may retain residual large-scale signals. As $v'$ contains only mesoscale variability, however, the covariances $\overline{v'\,T'}$ and $\overline{v'\,S'}$ primarily reflect eddy-induced transport, with any residual correlation with large-scale signals expected to be negligible after temporal and spatial averaging. This is

confirmed by sensitivity tests using reanalysis data, showing minimal differences both in spatial patterns and zonally integrated eddy fluxes with and without explicit spatial high-pass filtering of $T'$ and $S'$ (Supplementary Figure S5).

Uncertainties arising from uneven Argo sampling are quantified as follows. At each 2° × 2° grid point, the standard error is calculated from the ensemble of Argo profile-based eddy flux estimates. Errors are then propagated through zonal integration, assuming independence across longitudes and combining as the square root of the sum of squares, and through depth integration, assuming correlation across depths and summing directly, yielding a latitude-dependent standard error (Figures 3c and 4c). Given that typical eddy diameters of 100–400 km (Chelton et al., 2011) are comparable to the 2° grid spacing (~200 km), zonal integration errors are likely underestimated due to spatial correlations between adjacent grid boxes, with an underestimation factor of at about $\sqrt{2}$. The reported uncertainty should therefore be interpreted as a lower bound of the true sampling error.

**2.5 Estimation of oceanic total heat and salt transports**

Assuming that the long-term global ocean heat and freshwater budgets are approximately balanced, ocean circulation-driven transports must balance the forcing by surface heat and freshwater fluxes. Therefore, the total meridional heat and salt transports in the ocean are estimated by integrating the net surface heat flux ($Q_{net}$) and freshwater flux ($F_{net}$) from the southern to the northern hemisphere (Large and Yeager, 2009; Tréguier et al., 2014), taking Antarctica ($y = y_s$) as the southern boundary:

$$Q_t(y) = \int_{y_s}^{y} \int_{x_w}^{x_e} Q_{net}\, dx\, dy, \qquad (7)$$

$$F_t(y) = S_0 \int_{y_s}^{y} \int_{x_w}^{x_e} F_{net}\, dx\, dy, \qquad (8)$$

where $S_0 = 35$ PSU is a reference salinity used to convert freshwater flux to salt transport. Positive value denotes northward transport and negative value indicates southward transport. A globally uniform correction of 2.0 W/m$^2$ is applied to $Q_{net}$ and 7.3 x 10$^{-10}$ m/s to $F_{net}$ to remove the overall bias, ensuring zero flux at the northern boundary and preserving global conservation. These corrections are small relative to the climatological background and do not alter the main spatial patterns (Figures 3d and 4d).

## 3. Results

### 3.1 Contrasting vertical structures of meridional eddy heat and salt transports

Meridional eddy heat and salt transports are strongest in energetic regions such as western boundary currents and the Antarctic Circumpolar Current, with this feature becoming more pronounced at greater depths. Notably, eddy heat and salt transports exhibit distinct vertical patterns. Eddy heat transport shows a pronounced depth-dependent reversal—a feature rarely highlighted in previous studies. Near the sea surface, it is predominantly poleward—northward in the Northern Hemisphere and southward in the Southern Hemisphere, consistent with previous estimates based on satellite observations (Figure 1a; Guo et al., 2022; Chen & Yu, 2024). As depth increases, however, the transport gradually weakens and reverses to equatorward, which is particularly pronounced within the subtropical gyres between 5° and 40° latitudes (Figures 1b and c).

In contrast, the eddy salt transport exhibits a prominent latitude-dependent pattern. Near the surface, meridional eddy salt transport displays clear zonal bands: equatorward at low latitudes, poleward at mid-latitudes, and weakly equatorward at high latitudes (Figure 1d). With increasing depth, the equatorward salt transport rapidly weakens, leaving a dominant poleward transport in the mid-latitudes that extends below 800 m (Figures 1e and f). Notably, the direction of the eddy salt transport reverses near 800 m in the northern Pacific Ocean, corresponding to a change in the meridional salinity gradient (Supplementary Figure S8). These distinct depth- and latitude-dependent features highlight the distinct behaviors of eddy heat and salt transports across the global ocean.

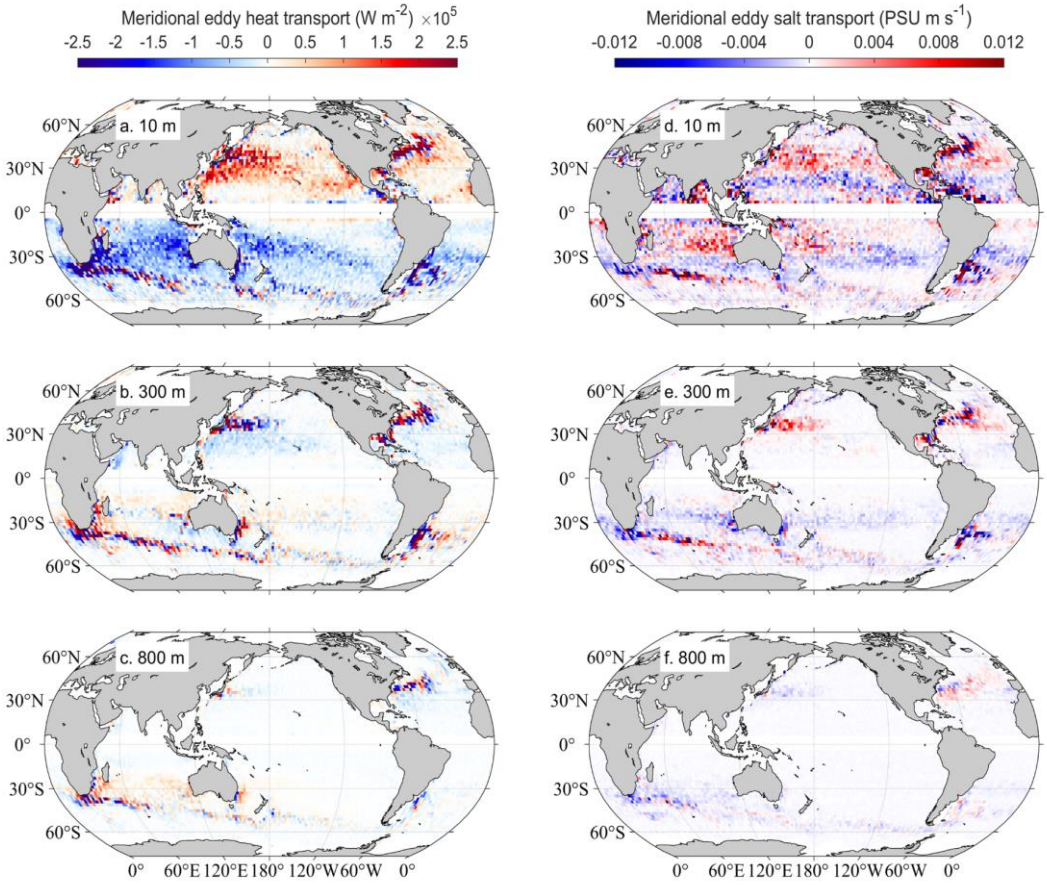


**Figure 1.** Global distributions of time-mean meridional eddy heat transport (a–c) and eddy salt transport (d–f) at depths of 10, 300, and 800 m.

The zonally integrated latitude–depth sections further illustrate the distinct vertical structures of meridional eddy heat and salt transports (Figure 2). Both eddy fluxes are largely confined to the upper 1000 m, exhibiting shallow structures at low and high latitudes but deeper penetration at mid-latitudes. The eddy heat transport clearly reverses direction with depth—poleward in the upper few hundred meters and equatorward at greater depths. This vertical reversal is evident across all three major ocean basins between 40° S and 40° N (Figures 2a-d). The depth of this reversal increases systematically with latitude, ranging from about 100 m in the tropics to nearly 300 m in the subtropics.

In contrast, meridional eddy salt transport depends primarily on latitude rather than depth (Figures 2e–h). In the tropics, eddy salt transport is equatorward and mainly confined to the upper 300 m. At mid-latitudes, a pronounced reversal occurs, with strong poleward transport extending from the surface to about 1000 m. At high latitudes, weak equatorward transport persists,

particularly in the Indian Ocean section of the Antarctic Circumpolar Current (Figures 2f, 4a). These results underscore the fundamentally distinct vertical and latitudinal behaviors of meridional eddy heat and salt transports.

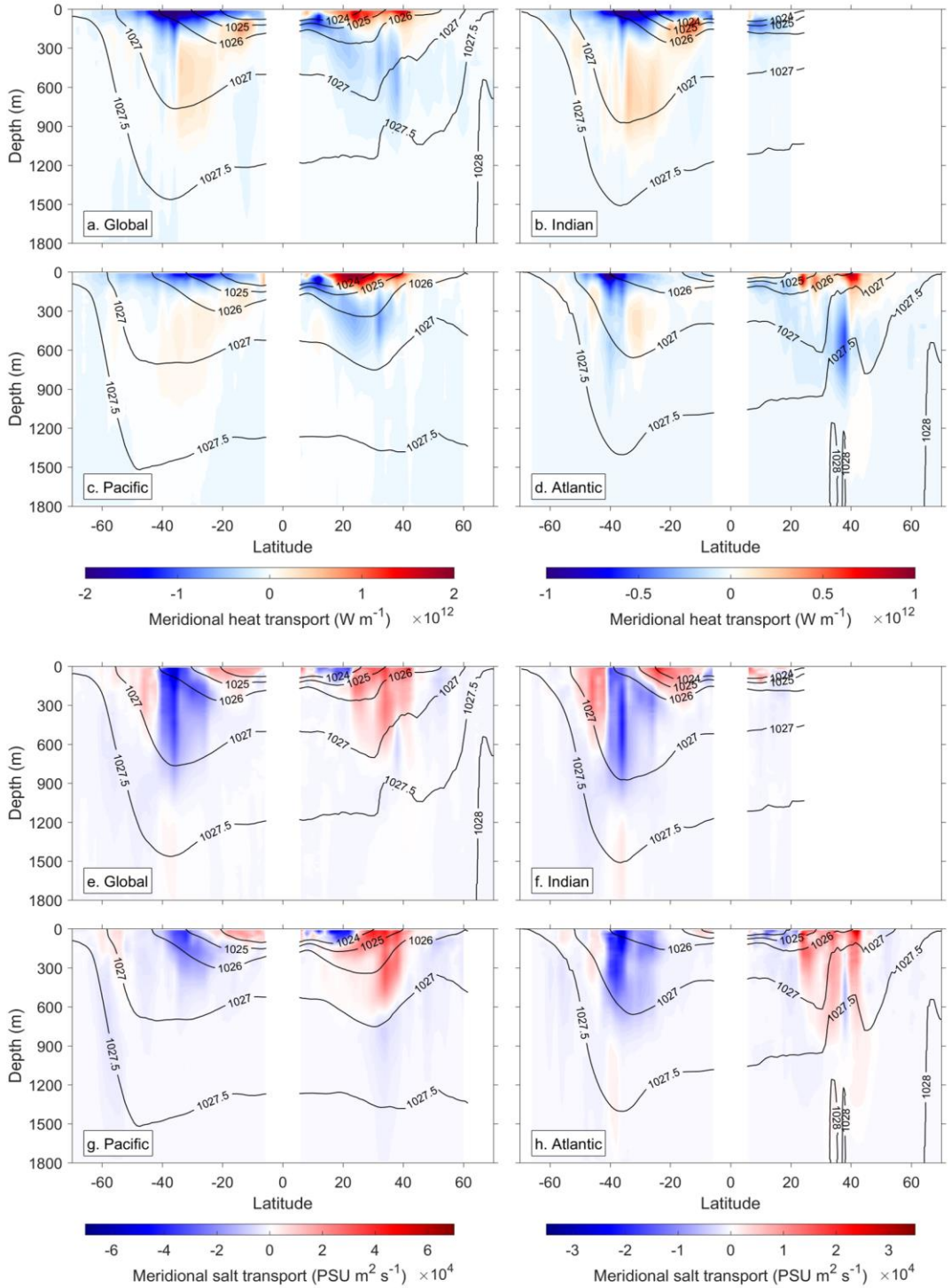


**Figure 2.** Latitude–depth distributions of zonally integrated meridional eddy heat transport for (a) the global ocean, (b) Indian Ocean, (c) Pacific Ocean, and (d) Atlantic Ocean. (e-f) Same as (a-d), but for eddy salt transport. Contours show zonally averaged climatological isopycnals. The left- and right-hand colorbars apply to the global

ocean and regional basins, respectively.

### 3.2 Eddy contributions to global ocean heat and salt budgets

Depth- and zonally integrated meridional eddy heat and salt transports reflect the cumulative effects of mesoscale eddies on large-scale climate regulation. Compared with individual-depth patterns, the vertically integrated eddy heat transport field appears considerably noisier (Figure 3a). In the subtropical gyres, poleward fluxes in the upper ocean and equatorward fluxes at depth largely cancel out each other, resulting in a weak net equatorward transport. In contrast, pronounced depth-integrated eddy heat transport occurs along the western boundary currents and the Antarctic Circumpolar Current. These regions exhibit alternating positive and negative values of eddy heat fluxes, consistent with previous observational and modeling studies (Qiu & Chen, 2005; Jayne & Marotzke, 2002; Zhang et al., 2014b). This pattern is likely associated with rotational eddy fluxes (Marshall & Shutts, 1981; Eden et al., 2007) that partially cancel each other out when zonally integrated.

With some fluctuations, the zonally- and depth-integrated meridional eddy heat transport is directed equatorward between 38°S and 38°N and is poleward out of these latitudes, leading to heat convergence at low latitudes and divergence at mid-latitudes (Figure 3b). Its magnitude ranges from −0.45 to +0.20 PW, with peak values near 40° in both hemispheres, corresponding to the Antarctic Circumpolar Current and western boundary currents. Cancellation between upper-ocean poleward and deep equatorward fluxes renders tropical and subtropical transport relatively weak ($\pm$0.12 PW). Among the three major ocean basins, the Atlantic Ocean contributes the most to global meridional eddy heat transport, followed by the Indian Ocean, with the Pacific Ocean contributing the least (Figure 3c).

To further quantify the contribution of mesoscale eddies to the global ocean heat balance, we compare the zonally- and depth-integrated eddy heat transport with total meridional heat transport derived from net surface heat flux (Figures 3d–f; see Methods). On average, the ocean gains heat at low latitudes and loses it at high latitudes, producing poleward total heat transport in both hemispheres. Between 5° and 38° latitude in both hemispheres, however, eddy heat transport is equatorward, opposing the large-scale circulation. Beyond 38° latitude, eddy heat transport shifts

poleward, aligning with the large-scale circulation and thereby amplifying the total meridional ocean heat flux. This reinforcing effect is most pronounced at mid-latitudes, particularly within a narrow band of the Southern Ocean around 40°S. Collectively, these results demonstrate that mesoscale eddies exert a latitude-dependent influence on the global ocean heat balance—reducing poleward transport in the subtropics while enhancing it at mid- and high latitudes.

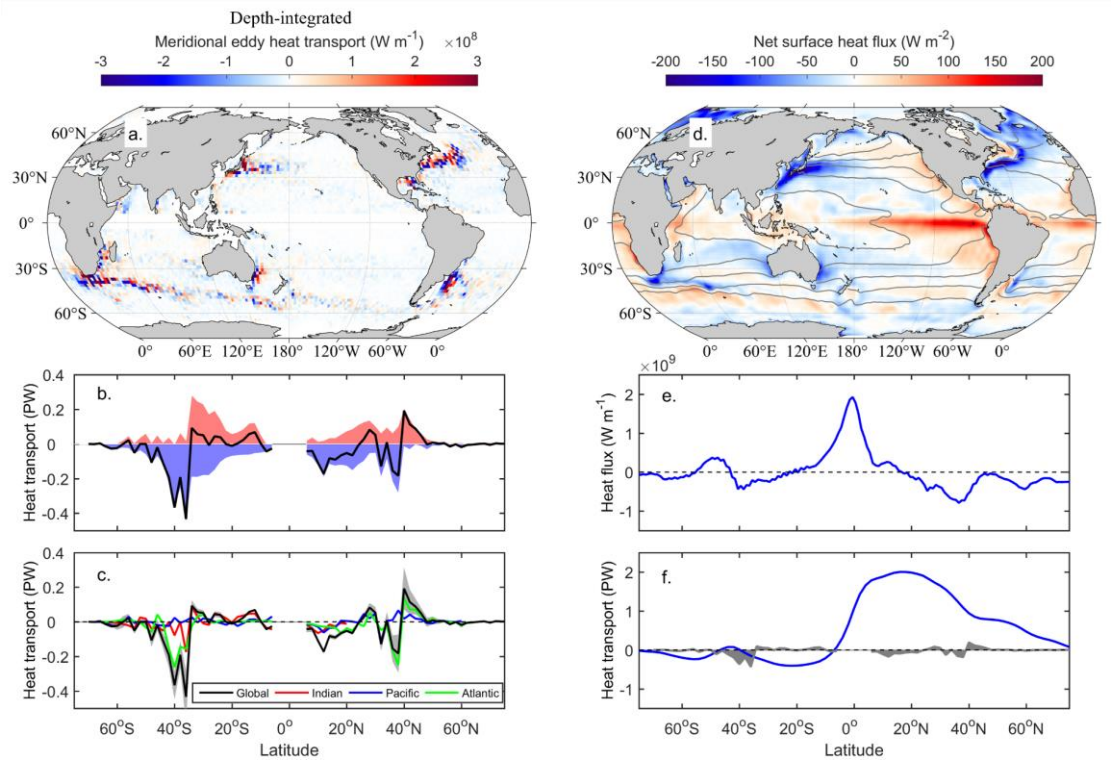


**Figure 3.** (a) Depth-integrated meridional eddy heat transport. (b) Zonally and depth-integrated meridional eddy heat transport (PW, 1 PW = $10^{15}$ W). Red and blue shading indicate positive and negative contributions, respectively, and black curve shows their sum. (c) Zonally and depth-integrated meridional heat transport for the global ocean (black), Indian Ocean (red), Pacific Ocean (blue), and Atlantic Ocean (green). Gray shading indicates the sampling error of the global estimate (see Methods). (d) Climatological net surface heat flux, with gray contours showing sea surface temperature at 5 °C intervals. (e) Zonally integrated net surface heat flux. (f) Contribution of eddy heat transport to the global ocean heat budget. Blue line shows the total time-mean heat transport derived from net surface heat flux, and gray shading represents the zonally and depth-integrated eddy heat transport.

Compared with the eddy heat transport, the depth-integrated eddy salt transport exhibits a clearer and more coherent pattern because its vertically consistent transport direction minimizes cancellation during integration (Figures 4a, b). The zonally- and depth-integrated eddy salt

transport is equatorward at low and high latitudes, but strongly poleward across a broad mid-latitude band (~20°–40°). This induces salt convergence in the tropics and subpolar regions, but divergence in the subtropics. The equatorward eddy salt transport is relatively weak (within ±5 PSU·Sv), whereas the poleward transport is much stronger, peaking at about −30 PSU·Sv in the Southern Hemisphere and +15 PSU·Sv in the Northern Hemisphere. The Pacific, Atlantic, and Indian Oceans all contribute significantly to the global meridional eddy salt transport (Figure 4c).

We further compare eddy salt transport with the total meridional salt transport (Figures 4d–f). In the Intertropical Convergence Zone and from mid- to high latitudes, precipitation exceeds evaporation, leading to relatively low sea surface salinity. By contrast, evaporation dominates in the subtropical gyres, producing pronounced salinity maxima (Figures 4d, e). This spatially heterogeneous pattern of net freshwater flux requires compensation by oceanic processes, which redistribute salt by transporting saline waters from the subtropics to the equator and poles (Figure 4f). The eddy salt transport operates in tandem with the mean flow to offset the salinity imbalance imposed by surface freshwater forcing. Its contribution is particularly strong at mid-latitudes, accounting for nearly ~50 % of the total meridional ocean salt transport. These results highlight the key role of mesoscale eddies in the global salt balance.

Sampling errors are largest at mid-latitudes, where eddy transports are strongest, and smaller at low and high latitudes (Figures 3c, 4c). Overall, uncertainties are generally less than 0.08 PW for eddy heat transport and 5 PSU·Sv for eddy salt transport, small relative to the signals and thus not affecting the main conclusions.

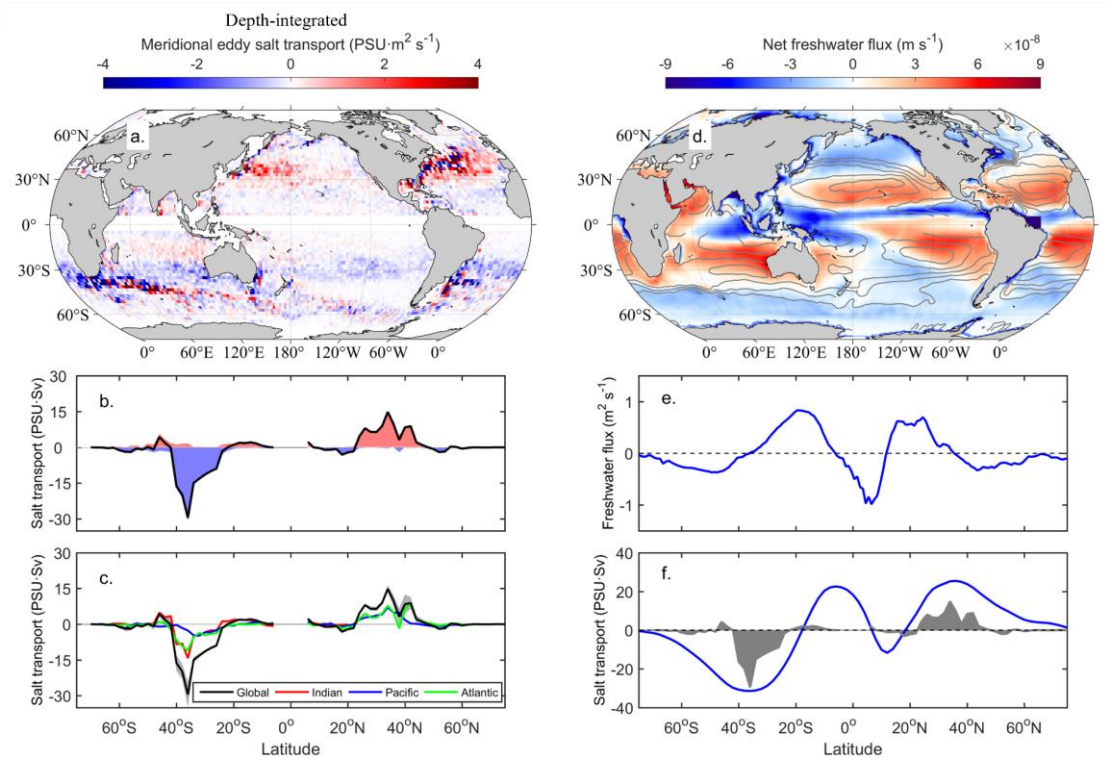


**Figure 4.** (a) Depth-integrated meridional eddy salt transport. (b) Zonally and depth-integrated meridional salt transport (PSU•Sv, 1 Sv = $10^6$ m$^3$ s$^{-1}$). Red and blue shading indicate positive and negative contributions, respectively, and black curve shows their sum. (c) Zonally and depth-integrated meridional salt transport for the global ocean (black), Indian Ocean (red), Pacific Ocean (blue), and Atlantic Ocean (green). Gray shading indicates the sampling error of the global estimate. (d) Climatological net freshwater flux (evaporation – precipitation – runoff). Gray contours show climatological sea surface salinity at 0.5 PSU intervals. (e) Zonally integrated net freshwater flux. (f) Contribution of eddy salt transport to the global ocean salt budget. Blue line shows the total time-mean salt transport derived from net freshwater flux, and gray shading represents the zonally and depth-integrated eddy salt transport.

## 4. Discussion and Conclusions

Mesoscale eddy heat and salt transports play a key role in regulating regional and global climate. By combining satellite altimetry with Argo observations, we estimate the global 3D meridional eddy heat and salt transports, revealing strikingly distinct vertical structures. Eddy heat transport reverses with depth, leading to strong vertical cancellation and a weak net contribution to the total meridional heat transport. In contrast, eddy salt transport exhibits pronounced latitude dependence, being weak and equatorward at low latitudes but strong and poleward at mid-latitudes, contributing significantly to the global meridional salt transport.

To assess the robustness of our reconstructed 3D eddy transports, we applied two additional independent approaches (Methods in Supporting Information). First, the composite eddy structure was replaced with an analytical surface mode. This yields slightly stronger subsurface eddy heat and salt transports (Supplementary Figures S6c, d), largely due to the more gradual vertical decay of the surface mode compared to the composite eddy structure (Ni et al., 2023). Second, the eddy heat and salt transports were directly computed from the covariance of temperature (or salinity) and velocity anomalies using an ocean reanalysis product. This method reproduces the key vertical features of both eddy heat and salt transports, with only minor regional deviations (Supplementary Figures S6e, f). Overall, the three approaches produce similar magnitudes and patterns of eddy-induced transports, confirming the reliability of our results.

The different vertical structure of eddy heat and salt transports primarily reflect the background temperature and salinity gradients, which govern the direction of the eddy fluxes (Supplementary Figures S7, S8). Near the surface, temperature decreases from the equator to the poles, and the corresponding down-gradient eddy heat transport is poleward in both hemispheres. With increasing depth, the temperature maximum shifts from the equator to the subtropics, reversing the background temperature gradient and thus the direction of eddy heat transport at low latitudes. In contrast, the evaporation–precipitation asymmetry generates salinity maxima in the subtropical gyres, producing an equatorward gradient at low latitudes and a poleward gradient at mid- and high latitudes. The background salinity gradient varies little with depth, resulting in a vertically consistent down-gradient eddy salt transport.

These findings provide a valuable benchmark for evaluating ocean climate models. It remains unclear whether coarse-resolution ocean models employing eddy parameterizations (Gent and McWilliams, 1990; Gent et al., 1995; Hewitt et al., 2020) can represent these distinct eddy heat and salt transport structures identified here. The predominantly down-gradient eddy transport pattern highlights the importance of accurately simulating background temperature and salinity gradients. A systematic assessment of model performance is left for future work.

Our eddy transport estimates include contributions from both eddy trapping and eddy stirring. Although a dedicated Lagrangian analysis to separate these effects is beyond the scope of this study, recent studies suggest that eddy stirring dominates global eddy transport, exceeding the

contribution from coherent eddy trapping by one to two orders of magnitude (Sun et al., 2019; Yang et al., 2025; Yuan et al., 2025).

In summary, this study provides an observationally constrained view of global 3D eddy heat and salt transports, highlights their distinct roles in the climate system, and offers insights for improving the representation of mesoscale processes in future ocean and climate models.

## Conflict of Interest

The authors declare no conflicts of interest relevant to this study.

## Acknowledgements

This work is supported by the National Natural Science Foundation of China (42430401, 42576009), the Southern Marine Science and Engineering Guangdong Laboratory (Guangzhou) (SML2023SP207), and the Chinese Academy of Sciences (XDA0370100, XDA0370101).

## Data availability

The satellite altimeter SLA data is available from CMEMS (European Union-Copernicus Marine Service, 2021). The Argo dataset is provided by China Argo Real-time data center (https://www.argo.org.cn/english/), and these data were collected and made freely available by the International Argo Program and the national programs that contribute to it (Argo, 2026). CORE.2 Global Air-Sea Flux Dataset is available from the National Center for Atmospheric Research Geoscience Data Exchange (Yeager & Large, 2008). We appreciate the provision of these publicly available datasets.

## References

Abernathey, R., & Haller, G. (2018). Transport by Lagrangian vortices in the eastern Pacific. *Journal of Physical Oceanography*, *48*(3), 667–685. https://doi.org/10.1175/JPO-D-17-0102.1

Aiki, H., Zhai, X., & Greatbatch, R. J. (2016). Energetics of the global ocean: The role of

mesoscale eddies. *In Indo-Pacific Climate Variability and Predictability* (pp. 109–134). https://doi.org/10.1142/9789814696623_0004

Argo (2026). Argo float data and metadata from Global Data Assembly Centre (Argo GDAC) [Dataset]. SEANOE. https://doi.org/10.17882/42182

Beech, N., et al. (2022). Long-term evolution of ocean eddy activity in a warming world. *Nature Climate Change*, *12*, 910–917. https://doi.org/10.1038/s41558-022-01478-3

Chaigneau, A., Texier, M. L., Eldin, G., Grados, C., & Pizarro, O. (2011). Vertical structure of mesoscale eddies in the eastern South Pacific Ocean: A composite analysis from altimetry and Argo profiling floats. *Journal of Geophysical Research: Oceans*, *116*, C11025. https://doi.org/10.1029/2011JC007134

Chassignet, E. P., et al. (2020). Impact of horizontal resolution on global ocean–sea-ice model simulations based on OMIP-2 experimental protocols. *Geoscientific Model Development*, *13*, 4595–4626. https://doi.org/10.5194/gmd-13-4595-2020

Chelton, D. B., Schlax, M. G., & Samelson, R. M. (2011). Global observations of nonlinear mesoscale eddies. *Progress in Oceanography*, *91*, 167–216. https://doi.org/10.1016/j.pocean.2011.01.002

Chen, Y., & Yu, L. (2024). Mesoscale meridional heat transport inferred from sea surface observations. *Geophysical Research Letters*, *51*, e2023GL106376. https://doi.org/10.1029/2023GL106376

de La Lama, M. S., LaCasce, J. H., & Fuhr, H. K. (2016). The vertical structure of ocean eddies. Dynamics and Statistics of the Climate System, 2, dzw001. https://doi.org/10.1093/climsys/dzw001

Delman, A., & Lee, T. (2021). Global contributions of mesoscale dynamics to meridional heat transport. *Ocean Science*, *17*, 1031–1049. https://doi.org/10.5194/os-17-1031-2021

Ding, M., et al. (2022). Overestimated eddy kinetic energy in the eddy-rich regions simulated by eddy-resolving global ocean–sea ice models. *Geophysical Research Letters*, *49*, e2022GL098370. https://doi.org/10.1029/2022GL098370

Dong, C., McWilliams, J. C., Liu, Y., & Chen, D. (2014). Global heat and salt transports by eddy movement. *Nature Communications*, *5*, 3294. https://doi.org/10.1038/ncomms4294

Dong, D., et al. (2017). Mesoscale eddies in the northwestern Pacific Ocean: Three-dimensional eddy structures and heat/salt transports. *Journal of Geophysical Research: Oceans*, *122*, 9795–9813. https://doi.org/10.1002/2017JC013303

Dufour, C. O., Griffies, S. M., de Souza, G. F., Frenger, I., Morrison, A. K., Palter, J. B., & Slater, R. D. (2015). Role of mesoscale eddies in cross-frontal transport of heat and biogeochemical tracers in the Southern Ocean. *Journal of Physical Oceanography*, *45*, 3057–3081. https://doi.org/10.1175/JPO-D-14-0240.1

Eden, C., Greatbatch, R. J., & Olbers, D. (2007). Interpreting eddy fluxes. *Journal of Physical Oceanography*, *37*, 1282–1296. https://doi.org/10.1175/JPO3050.1

European Union-Copernicus Marine Service. (2021). GLOBAL OCEAN GRIDDED L4 SEA SURFACE HEIGHTS AND DERIVED VARIABLES REPROCESSED (1993-ONGOING) [Dataset]. *Mercator Ocean International*. https://doi.org/10.48670/MOI-00148

Frenger, I., Münnich, M., Gruber, N., & Knutti, R. (2015). Southern Ocean eddy phenomenology. *Journal of Geophysical Research: Oceans*, *120*, 7413–7449. https://doi.org/10.1002/2015JC011047

Gent, P. R., & McWilliams, J. C. (1990). Isopycnal mixing in ocean circulation models. Journal of Physical Oceanography, 20(1), 150–155. https://doi.org/10.1175/1520-0485(1990)020<0150:IMIOCM>2.0.CO;2

Gent, P. R., Willebrand, J., McDougall, T. J., & McWilliams, J. C. (1995). Parameterizing eddy-induced tracer transports in ocean circulation models. Journal of Physical Oceanography, 25(4), 463–474. https://doi.org/10.1175/1520-0485(1995)025<0463:PEITTI>2.0.CO;2

Griffies, S. M., et al. (2015). Impacts on ocean heat from transient mesoscale eddies in a hierarchy of climate models. *Journal of Climate*, *28*, 952–977. https://doi.org/10.1175/JCLI-D-14-00353.1

Guo, Y., Bachman, S., Bryan, F. O., & Bishop, S. (2022). Increasing trends in oceanic surface poleward eddy heat flux observed over the past three decades. *Geophysical Research Letters*, *49*, e2022GL099362. https://doi.org/10.1029/2022GL099362

Hewitt, H. T., Roberts, M., Mathiot, P., et al. (2020). Resolving and parameterising the ocean mesoscale in Earth system models. Current Climate Change Reports, 6, 137–152.

https://doi.org/10.1007/s40641-020-00164-w

Isern-Fontanet, J., Lapeyre, G., Klein, P., Chapron, B., & Hecht, M. W. (2008). Three-dimensional reconstruction of oceanic mesoscale currents from surface information. *Journal of Geophysical Research: Oceans*, *113*, C09005. https://doi.org/10.1029/2007JC004692

Jayne, S. R., & Marotzke, J. (2002). The oceanic eddy heat transport. *Journal of Physical Oceanography*, *32*, 3328–3345. https://doi.org/10.1175/1520-0485(2002)032<3328:TOEHT>2.0.CO;2

LaCasce, J. H. (2012). Surface quasigeostrophic solutions and baroclinic modes with exponential stratification. *Journal of Physical Oceanography*, *42*, 569–580. https://doi.org/10.1175/JPO-D-11-0111.1

LaCasce, J. H. (2017). The prevalence of oceanic surface modes. *Geophysical Research Letters*, *44*, 11097–11105. https://doi.org/10.1002/2017GL075430

LaCasce, J. H., & Groeskamp, S. (2020). Baroclinic modes over rough bathymetry and the surface deformation radius. *Journal of Physical Oceanography*, *50*, 2835–2847. https://doi.org/10.1175/JPO-D-20-0055.1

LaCasce, J. H., & Mahadevan, A. (2006). Estimating subsurface horizontal and vertical velocities from sea-surface temperature. *Journal of Marine Research*, *64*, 695–721. https://doi.org/10.1357/002224006779367267

Large, W., & Yeager, S. G. (2009). The global climatology of an interannually varying air–sea flux data set. Climate Dynamics, *33*, 341–364. https://doi.org/10.1007/s00382-008-0441-3

Li, X., et al. (2025). Oceanic uptake of $CO_2$ enhanced by mesoscale eddies. *Science Advances*, *11*, eadt4195. https://doi.org/10.1126/sciadv.adt4195

Liu, T., He, Y., Zhai, X., & Liu, X. (2022). Diagnostics of coherent eddy transport in the South China Sea based on satellite observations. *Remote Sensing*, *14*, 1690. https://doi.org/10.3390/rs14071690

Marshall, J., & Shutts, G. (1981). A note on rotational and divergent eddy fluxes. *Journal of Physical Oceanography*, *11*, 1677–1680. https://doi.org/10.1175/1520-0485(1981)011<1677:ANORAD>2.0.CO;2

Melnichenko, O., Hacker, P., & Müller, V. (2021). Observations of mesoscale eddies in satellite

SSS and inferred eddy salt transport. *Remote Sensing*, *13*, 315. https://doi.org/10.3390/rs13020315

Mo, D., He, Q., Zhan, W., He, Y., & Zhan, H. (2024). A global assessment of eddy-induced salinity anomalies and salt transport by eddy movement. *Journal of Geophysical Research: Oceans*, *129*, e2023JC020382. https://doi.org/10.1029/2023JC020382

Ni, Q., Zhai, X., LaCasce, J. H., Chen, D., & Marshall, D. P. (2023). Full-depth eddy kinetic energy in the global ocean estimated from altimeter and Argo observations. *Geophysical Research Letters*, *50*, e2023GL103114. https://doi.org/10.1029/2023GL103114

Pascual, A., Faugère, Y., Larnicol, G., & Le Traon, P.-Y. (2006). Improved description of the ocean mesoscale variability by combining four satellite altimeters. *Geophysical Research Letters*, *33*, L02611. https://doi.org/10.1029/2005GL024633

Qiu, B., & Chen, S. (2005). Eddy-induced heat transport in the subtropical North Pacific from Argo, TMI, and altimetry measurements. *Journal of Physical Oceanography*, *35*, 458–473. https://doi.org/10.1175/JPO2696.1

Steinberg, J. M., Yankovsky, E., Cole, S. T., & Zanna, L. (2025). A landscape of mesoscale eddy vertical structure: The influence of bathymetric slope and roughness on kinetic energy. *Journal of Physical Oceanography*, *55*, 1987–2004. https://doi.org/10.1175/JPO-D-25-0044.1

Sun, B., Liu, C., & Wang, F. (2019). Global meridional eddy heat transport inferred from Argo and altimetry observations. *Scientific Reports*, *9*, 1345. https://doi.org/10.1038/s41598-018-38069-2

Tréguier, A. M., et al. (2014). Meridional transport of salt in the global ocean from an eddy-resolving model. *Ocean Science*, *10*, 243–255. https://doi.org/10.5194/os-10-243-2014

Volkov, D. L., Lee, T., & Fu, L.-L. (2008). Eddy-induced meridional heat transport in the ocean. *Geophysical Research Letters*, *35*, L20601. https://doi.org/10.1029/2008GL035490

Wang, H., Qiu, B., Liu, H., & Zhang, Z. (2023). Doubling of surface oceanic meridional heat transport by non-symmetry of mesoscale eddies. *Nature Communications*, *14*, 5460. https://doi.org/10.1038/s41467-023-41294-7

Wunsch, C. (1997). The vertical partition of oceanic horizontal kinetic energy. *Journal of Physical*

*Oceanography*, *27*, 1770–1794. https://doi.org/10.1175/1520-0485(1997)027<1770:TVPOOH>2.0.CO;2

Xia, Q., Li, G., & Dong, C. (2022). Global oceanic mass transport by coherent eddies. *Journal of Physical Oceanography*, 52, 1111–1132. https://doi.org/10.1175/JPO-D-21-0103.1

Yang, Y., Zeng, L., Wang, Q., Shi, R., & Xiu, P. (2025). Imprints of eddy stirring and trapping effects on global salt transport. *Earth's Future*, *13*, e2024EF005330. https://doi.org/10.1029/2024EF005330

Yeager, S. G., & Large, W. G. (2008). CORE.2 Global Air-Sea Flux Dataset (update irregularly) [Dataset]. NSF National Center for Atmospheric Research. https://doi.org/10.5065/D6WH2N0S

Yuan, Q., Zhang, Z., Liu, T., Zhao, W., & Tian, J. (2025). Stirring by mesoscale eddies dominates meridional eddy heat transport in the global ocean. *Science China Earth Sciences*, *68*, 2904–2912. https://doi.org/10.1007/s11430-024-1653-8

Zhang, Z., Wang, W., & Qiu, B. (2014a). Oceanic mass transport by mesoscale eddies. *Science*, *345*, 322–324. https://doi.org/10.1126/science.1252418

Zhang, Z., Zhang, Y., Wang, W., & Huang, R. X. (2013). Universal structure of mesoscale eddies in the ocean. *Geophysical Research Letters*, *40*, 3677–3681. https://doi.org/10.1002/grl.50736

Zhang, Z., Zhong, Y., Tian, J., Yang, Q., & Zhao, W. (2014b). Estimation of eddy heat transport in the global ocean from Argo data. *Acta Oceanologica Sinica*, *33*, 42–47. https://doi.org/10.1007/s13131-014-0421-x